

## Electronic Supplementary Information

---

### Enhancing interfacial contact in all solid state batteries with a cathode-supported solid electrolyte membrane framework

Xinzhi Chen<sup>a</sup>, Wenjun He<sup>b</sup>, Liang-Xin Ding<sup>a</sup>, Suqing Wang<sup>a</sup>, Haihui Wang<sup>\*a</sup>

<sup>a</sup>School of Chemistry & Chemical Engineering, South China University of Technology, No. 381 Wushan Road, Guangzhou 510640, China.

Email: hhwang@scut.edu.cn

<sup>b</sup>Guangzhou FLM Scientific Instrument Co. Ltd

#### This ESI file includes:

Experimental Methods

Supplementary Text

Supplementary Table S1

Supplementary References S1 to S27

Supplementary Figures S1 to S17

#### Experimental Methods

##### *Preparation of the electrolyte slurry and the electrolyte membrane*

An appropriate amount of Al<sub>2</sub>O<sub>3</sub> (30 nm, Macklin Inc.), PEO (M<sub>n</sub> = 10<sup>6</sup>, Aladdin Inc.), PVDF (Arkema, Kynar 761) and LiTFSI (99.9 %, Macklin Inc.) were added into the N,N-DMF solvent, and the mixture was blended by a magnetic stirring for 24 h. Then homogeneous milky white slurry was ready for use (**Fig. S1**). The as prepared slurry was named as PPAL electrolyte slurry. For comparison, electrolyte slurry without PVDF was prepared and named as PAL electrolyte slurry. The separate solid electrolyte membrane was obtained by doctor blading the slurry on a

polytetrafluorethylene plate. Most of solvent was removed by drying in the air, and then the electrolyte membrane was further dried in the vacuum oven at 40 °C overnight. The free-standing membrane then can be peeled off from the polytetrafluorethylene plate. Finally the uniform electrolyte membrane was cut into circles with a diameter of 16 mm for use.

#### ***Preparation of the cathode supported composite polymer electrolyte membrane***

The cathode electrode was prepared by mixing LiFePO<sub>4</sub> (active material, 80 wt%), carbon (super-P, 10 wt%) and PPAL or PAL solid electrolyte (10 wt%, as binder) in N,N-DMF and vigorously stirring overnight. Homogeneous cathode slurry was then cast on an Al foil or a carbon coated Al foil using an Elcometer 4340 automatic film applicator. The tape was dried overnight at ambient condition. The electrolyte slurry was then cast on the dry cathode tape directly to form a cathode supported solid electrolyte membrane (as shown in **Fig. 2**). The integrated membrane was initially dried at ambient condition overnight, and then the residual solvent was completely removed by heating the membrane at 40 °C under vacuum overnight.

#### ***Battery assembly***

Solid state LiFePO<sub>4</sub>/Li batteries were assembled in an Ar filled glovebox without using any additional liquid electrolyte. Cathode supported SSLIBs were assembled by directly incorporating the cathode supported solid electrolyte membrane and a metal lithium sheet. Conventional SSLIBs were also fabricated by combining a separate cathode, a separate solid electrolyte membrane and a metal lithium sheet. Liquid lithium ion batteries were assembled using 2032 coin-type cells for comparison.

#### ***Characterizations***

In situ X-ray diffraction (XRD) patterns were collected on a Rigaku SmartLab SE (Cu-K $\alpha$ ) diffractometer from 30 to 60 °C (every 10 °C every step). Prior to collecting the pattern, the sample was held for at least 5 min at the set temperature to establish equilibrium. Thermal properties of solid electrolyte membranes were evaluated by thermogravimetric analysis and differential scanning calorimetry (TGA-DSC, Netzsch

STA 449 F5) at a heating rate of  $10\text{ }^{\circ}\text{C min}^{-1}$  from room temperature to  $800\text{ }^{\circ}\text{C}$  under Ar atmosphere. The Raman spectra were recorded with a Raman spectrometer (LabRAM Aramis).  $^{13}\text{C}$  solid state NMR measurements were carried out by a Bruker Avance III HD 400 spectrometer. A cross section polisher (Leica EM TIC 3X) was applied to prepare the cross section of the cathode supported solid electrolyte membrane. The cross section and the surface morphologies were examined using a scanning electron microscope (Hitachi SU8220) with an energy dispersive X-ray spectroscopy (EDX) unit. The electrochemical stability windows of the as prepared solid electrolyte membranes were determined by linear sweep voltammograms performed on a working electrode of stainless steel, with Li metal as the counter and reference electrode. The linear sweep voltammograms (LSV) were measured between 2 V and 6 V at a scan rate of  $0.5\text{ mV s}^{-1}$ . The ionic conductivities of the as prepared solid electrolytes were measured by a complex impedance method with a perturbation of 10 mV in the frequency range of  $10^6\text{ Hz}$ - $10^{-2}\text{ Hz}$  at various temperatures from 30 to  $80\text{ }^{\circ}\text{C}$ . The electrolyte membrane was sandwiched between a pair of stainless steel blocking electrodes with a diameter of 16 mm. The interfacial resistances were studied by means of AC impedance spectroscopy under frequencies from  $10^6$  to  $10^{-2}$  Hz with an oscillation voltage of 5 mV applied to  $\text{LiFePO}_4/\text{solid electrolyte}/\text{Li}$  cells at 30 and  $50\text{ }^{\circ}\text{C}$ . The electrochemical stability window, ionic conductivity and electrochemical impedance were conducted by electrochemical workstation (Gamry Interface 1000). The battery performances of SSLIBs were performed on a multichannel battery testing system (Neware Electronic Co., China) with cut-off voltages of 3.0 V (discharge) and 3.8 V (charge) at various current densities.

## **Supplementary Text**

### ***Physicochemical properties of the as prepared solid electrolytes***

Separate PPAL and PAL solid electrolyte membranes were prepared from a simple tape casting method. The ambient temperature XRD patterns of the pure  $\text{Al}_2\text{O}_3$ , pure PVDF, pure PEO, PPAL and PAL solid electrolyte membranes are shown in **Fig. S2a**

**and S2b.** Obviously, the degree of crystallinity of PEO in PAL solid electrolyte membrane is still high at ambient temperature. In contrast, the degree of crystallinity of PEO in PPAL solid electrolyte membrane decreases dramatically after adding PVDF. Trace amount of Al<sub>2</sub>O<sub>3</sub> phase can be found in both PAL and PPAL solid electrolyte membranes. To investigate the phase transition evolution with temperature, *in situ* XRD measurements were conducted from ambient temperature to 60 °C. As increasing the temperature, PAL solid electrolyte membrane delivers similar XRD patterns at 30 and 40 °C, while an amount of amorphous phases appear starting from 50 °C, indicating that there is a phase transition occurring at around 50 °C. Interestingly, when PAL solid electrolyte membrane was cooled back to 30 °C, the high temperature amorphous phase reverts to a crystalline state. On the contrary, PPAL solid electrolyte membrane always displays amorphous state from ambient temperature to 60 °C. Through comparing the composition of PAL and PPAL solid electrolytes, it is surmised that the addition of PVDF might be the cause for the crystalline variation of PEO at ambient temperature. Fluorescence from PPAL solid electrolyte sample can be found in Raman spectra (**Fig. S2c**), suggesting that conjugated structures may exist in PPAL solid electrolyte. It is noticed that there is no conjugated structure in both the bare PEO and PVDF, there must be some reactions happened between PEO and PVDF. But there is no new <sup>13</sup>C chemical shift found in PPAL solid electrolyte sample (**Fig. S2d**), indicating that either the background noise of solid state NMR is too strong or the reaction between PEO and PVDF is too slight. The specific mechanism will be studied later, because further discussion here would be beyond the scope of the work.

### ***Electrochemical stability windows and ionic conductivities***

The electrochemical stability window of the electrolyte is a crucial parameter which determines the practical application of the electrolyte in lithium ion batteries. Linear sweep voltammograms (LSV) were carried out to determine the electrochemical stability window by sandwiching the solid electrolyte membrane between a Li metal electrode and a stainless steel electrode. As shown in **Fig. S3a**, the PAL solid

electrolyte membrane is found to be more stable than that of PPAL solid electrolyte membrane at 50 °C. PAL and PPAL solid electrolyte membranes start to decompose due to oxidation beyond 5.08 V and 4.55 V, respectively. Since the cut off voltage of LiFePO<sub>4</sub>/Li batteries is 3.0 V (discharge) and 3.8 V (charge), thus the PAL and PPAL solid electrolyte membranes are stable enough in the LiFePO<sub>4</sub>/Li battery system.

The ionic conductivities of solid electrolytes were investigated via AC impedance spectroscopy measurements by sandwiching the solid electrolyte membrane between two stainless steel blocking electrodes. The electrochemical impedance spectra (EIS) of PAL and PPAL solid electrolyte membranes measured from 30 °C to 80 °C are presented in **Fig. S4** and **S5**. All impedance spectra display similar shapes. Depressed semicircles from high to intermediate frequencies can be attributed to the parallel combination of bulk resistance and capacitance of solid electrolyte <sup>1</sup>, while the linear behavior at low frequency might be associated with the interfacial double-layer capacitance between the electrode and the solid electrolyte <sup>2</sup>. The ionic conductivity ( $\sigma$ ) of solid electrolytes can be calculated from a resistance ( $R$ ) data measured at different temperatures using the following equation:

$$\sigma = \frac{L}{RS} \quad (1)$$

where  $L$  is the membrane thickness and  $S$  is the effective area of solid electrolyte membrane. The temperature dependence of the ionic conductivity for PAL and PPAL solid electrolyte membranes is shown in **Fig. S6**. Compared to the solid electrolyte without PVDF addition, PAL solid electrolyte shows a lower ionic conductivity than that of PPAL solid electrolyte at the low temperature region. As increasing the temperature, the ionic conductivity of PAL solid electrolyte increases faster than that of PPAL solid electrolyte before approaching 50 °C. The ionic conductivity of PAL solid electrolyte becomes higher than that of PPAL solid electrolyte when the temperature passes by 50 °C. The lower crystallinity normally results in more flexible local chains in amorphous zones, and eventually leads to a higher ionic conductivity <sup>3</sup>. <sup>4</sup>. In this study, we confirmed that the addition of PVDF can reduce the crystallinity of PEO matrix, as shown in XRD patterns in **Fig. S2a**. While without the addition of

PVDF, the PAL solid electrolyte still shows high crystallinity at ambient temperature, as shown in **Fig. S2b**. As a consequence, reduction of polymer crystallinity is the main reason for the conductivity improvement of the solid electrolytes at ambient temperature.

The Arrhenius plots of PAL and PPAL solid electrolyte membranes are shown in **Fig. S3b**. The activation energy ( $E_a$ ) can be calculated according to the classical Arrhenius relationship:

$$\sigma(T) = A \exp\left(-\frac{E_a}{RT}\right) \quad (2)$$

Where  $T$  is the absolute temperature, and  $A$  is the pre-exponential factor<sup>5,6</sup>. As for PAL solid electrolyte, it is clear that the slope for the changes in the ionic conductivities in the low temperature region (30 °C – 50 °C) is larger than that of the slope in the high temperature region (50 °C – 80 °C). Correspondingly, the activation energies in the low temperature region (30 °C – 50 °C) are around 79.846 kJ mol<sup>-1</sup>, and the activation energies in the high temperature region (50 °C – 80 °C) are around 34.068 kJ mol<sup>-1</sup>. This difference might be due to the amorphization of PEO from crystalline state to amorphous state when it is heated to the phase transition temperature at around 50 °C<sup>7-10</sup>, which is verified by the XRD results in **Fig. S2b**. On the contrary, PPAL solid electrolyte always keeps amorphous state from ambient temperature to 80 °C, the activation energies are around 32.494 kJ mol<sup>-1</sup>, which is comparable to the activation energies of PAL solid electrolyte in the high temperature region (50 °C - 80 °C). This result implies that Li ion transport through the amorphous electrolyte membrane is much faster than that of the crystalline electrolyte membrane.

### ***Thermal properties and DSC analysis***

Good thermal stability is a crucial property of polymer electrolytes used in SSLIBs, and was investigated by thermogravimetric measurement. As shown in **Fig. S3c**, the thermal degradation temperatures of PAL and PPAL solid electrolytes are about 381 and 351 °C, respectively, indicating that the thermal stability of PEO based solid electrolyte decreases along with the addition of PVDF. The minor weight loss of PEO based solid electrolytes before the thermal degradation might be ascribed to the

trapped moisture. It is worth to notice that the weight loss of PPAL solid electrolyte is larger than that of PAL solid electrolyte, which might be due to the higher amorphous fraction in PPAL solid electrolyte resulting from the interaction between PVDF, PEO, inorganic nanofiller and lithium salt <sup>11</sup>. However, the thermal stability of two solid electrolytes is good enough before their decomposition onset temperature, these two solid electrolytes are thus sufficient to be used in SSLIBs under the normal working conditions.

**Fig. S3d** shows DSC curves of PPAL and PAL solid electrolytes. An endothermic peak can be found at around 53 °C for PAL solid electrolyte, indicating a phase transition may occur at around 53 °C, which is consistent to previous report <sup>10</sup>. While the DSC curve of PPAL solid electrolyte displays no peak at around this temperature, suggesting that the PVDF-PEO blending polymer electrolyte maintains a steady phase state under the measurement condition. This finding is in a good agreement with XRD results in **Fig. S2a and S2b**. These results suggest that bare inorganic fillers are not enough to reduce the crystallinity of PEO matrix at ambient temperature, while the addition of PVDF can efficiently reduce the crystallinity. Lower crystallinity of solid polymer electrolyte membrane is beneficial for improving ionic conductivity<sup>12,13</sup>.

**Supplementary Table S1.**

Comparisons of electrochemical performances of all solid state lithium ion batteries based on  $\text{LiFePO}_4$  cathode material.

No.	Solid electrolytes	Working temperature (°C)	Discharge capacities ( $\text{mAh g}^{-1}$ )	Rate capability ( $\text{mAh g}^{-1}$ )	Ref.
1	<b>LITFSI-<math>\text{Al}_2\text{O}_3</math>-PEO</b>	<b>50</b>	<b>169 (0.05C)</b>	<b>36 (1C)</b>	<b>This work</b>
		<b>30</b>	<b>42 (0.05C)</b>	<b>/</b>	
	<b>LITFSI-<math>\text{Al}_2\text{O}_3</math>-PVDF-PEO</b>	<b>50</b>	<b>164 (0.1C)</b>	<b>107 (1C)</b>	
		<b>30</b>	<b>125 (0.1C)</b>	<b>/</b>	
2	$\text{LiSO}_3\text{CF}_3$ - $\text{ZrO}_2$ -PEO	100	160 (0.2C)	90 (1C)	S14
3	LiTFSI-2-(2-methoxyethoxy)-PEO	60	128 (C/24)	/	S15
4	$\text{LiSO}_3\text{CF}_3$ - $\text{ZrO}_2$ -PEO	100	138 (0.1C)	60 (1C)	S16
5	$\text{LiPF}_6$ - $\text{MgAl}_2\text{O}_4$ -PEO	70	150 (0.1C)	130 (1C)	S17
6	P(STFSILi)-b-PEO	80	165 (C/15)	138 (2C)	S18
7	LiTFSI-PTMC	60	153 (C/55)	/	S19
8	LiTFSI-LGPS-PEO	60	158 (0.1C)	99 (1C)	S8
9	LiTFSI-LLZTO-PEO	60	~152 (0.1C)	/	S20
10	$\text{LiClO}_4$ -PEO	65	~126 (0.1C)	/	S21
11	$\text{LiClO}_4$ - $\text{ZrO}_2$ -PEO	90	~150 (C/7)	/	S22
		60	~60 (C/7)		
		51	~30 (C/7)		
12	LAGP-PEO	55	138 (0.1C)	95 (2C)	S23
		25	20 (0.1C)	/	
13	LiTFSI-LLZO-PEO	60	150 (0.1C)	100 (1C)	S24
14	(LiTFSI- $\text{Al}_2\text{O}_3$ -CPEO)+LLZT	65	142 ( $80 \mu\text{A cm}^{-2}$ )	/	S25
15	PEO+LLTO	65	127 (0.05C)	/	S26
16	$\text{Li}_2(\text{OH})_{0.9}\text{F}_{0.1}\text{Cl}$	65	125 (0.2C)	/	S27

Remarks: Polymer solid electrolytes: No. 1 to No. 13

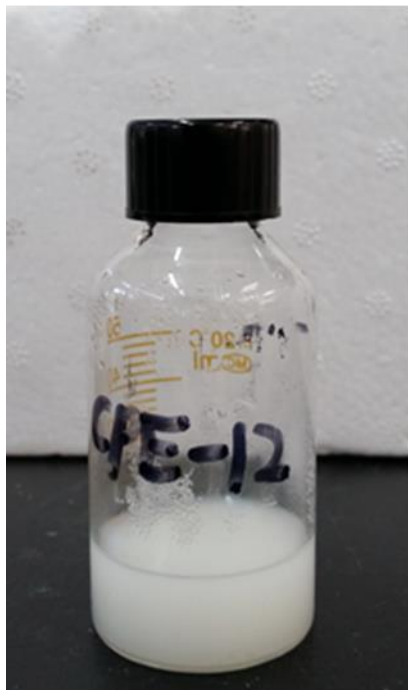
Inorganic solid electrolytes: No. 14 to No. 16.

## Supplementary References

- S1. J. Cardoso, D. Nava, P. García-Morán, F. Hernández-Sánchez, B. Gomez, J. Vazquez-Arenas and I. González, *J. Phys. Chem. C*, 2015, **119**, 4655.
- S2. W. Liu, N. Liu, J. Sun, P. C. Hsu, Y. Li, H. W. Lee and Y. Cui, *Nano Lett.*, 2015, **15**, 2740.
- S3. F. Croce, G. B. Appetecchi, L. Persi and B. Scrosati, *Nature*, 1998, **394**, 456.
- S4. J. Xi and X. Tang, *Chem. Phys. Lett.*, 2004, **393**, 271.
- S5. C. W. Kuo, C. W. Huang, B. K. Chen, W. B. Li, P. R. Chen, T. H. Ho, C. G. Tseng and T. Y. Wu, *Int. J. Electrochem. Sci.*, 2013, **8**, 3834.
- S6. F. Croce, M. L. Focarete, J. Hassoun, I. Meschini and B. Scrosati, *Energy Environ. Sci.*, 2011, **4**, 921.
- S7. J.-H. Choi, C.-H. Lee, J.-H. Yu, C.-H. Doh and S.-M. Lee, *J. Power Sources*, 2015, **274**, 458.
- S8. Y. Zhao, C. Wu, G. Peng, X. Chen, X. Yao, Y. Bai, F. Wu, S. Chen and X. Xu, *J. Power Sources*, 2016, **301**, 47.
- S9. S. K. Fullerton-Shirey and J. K. Maranas, *J. Phys. Chem. C*, 2010, **114**, 9196.
- S10. R. Prasanth, N. Shubha, H. H. Hng and M. Srinivasan, *J. Power Sources*, 2014, **245**, 283.
- S11. W.-H. Hou, C.-Y. Chen, C.-C. Wang and Y.-H. Huang, *Electrochim. Acta*, 2003, **48**, 679-690.
- S12. W. Krawiec, L. G. Scanlon, J. P. Fellner, R. A. Vaia, S. Vasudevan and E. P. Giannelis, *J. Power Sources*, 1995, **54**, 310.
- S13. S. Srivastava, J. L. Schaefer, Z. Yang, Z. Tu and L. A. Archer, *Adv. Mater.*, 2014, **26**, 201.
- S14. F. S. Fiory, F. Croce, A. D'Epifanio, S. Licoccia, B. Scrosati and E. Traversa, *J. Eur. Ceram. Soc.*, 2004, **24**, 1385.
- S15. Y. Kobayashi, S. Seki, Y. Mita, Y. Ohno, H. Miyashiro, P. Charest, A. Guerfi and K. Zaghib, *J. Power Sources*, 2008, **185**, 542.
- S16. L. Damen, J. Hassoun, M. Mastragostino and B. Scrosati, *J. Power Sources*, 2010, **195**, 6902.
- S17. N. Angulakshmi, K. S. Nahm, J. R. Nair, C. Gerbaldi, R. Bongiovanni, N. Penazzi and A. M. Stephan, *Electrochim. Acta*, 2013, **90**, 179.
- S18. R. Bouchet, S. Maria, R. Meziane, A. Aboulaich, L. Lienafa, J.-P. Bonnet, T. N. T. Phan, D. Bertin, D. Gimes, D. Devaux, R. Denoyel and M. Armand, *Nat. Mater.*, 2013, **12**, 452.
- S19. B. Sun, J. Mindemark, K. Edström and D. Brandell, *Solid State Ionics*, 2014, **262**, 738.
- S20. C. Z. Zhao, X. Q. Zhang, X. B. Cheng, R. Zhang, R. Xu, P. Y. Chen, H. J. Peng, J. Q. Huang and Q. Zhang, *P. Natl. Acad. Sci. USA*, 2017, **114**, 11069.
- S21. L. Wang, X. Li and W. Yang, *Electrochim. Acta*, 2010, **55**, 1895.
- S22. F. Croce, S. Sacchetti and B. Scrosati, *J. Power Sources*, 2006, **162**, 685.
- S23. Y. C. Jung, S. M. Lee, J. H. Choi, S. S. Jang and D. W. Kim, *J. Electrochem. Soc.*, 2015, **162**, A704.
- S24. F. Chen, D. Yang, W. Zha, B. Zhu, Y. Zhang, J. Li, Y. Gu, Q. Shen, L. Zhang and D. R. Sadoway, *Electrochim. Acta*, 2017, **258**, 1106.
- S25. Y. Li, B. Xu, H. Xu, H. Duan, X. Lü, S. Xin, W. Zhou, L. Xue, G. Fu, A. Manthiram and J. B. Goodenough, *Angew. Chem. Int. Ed.*, 2016, **55**, 1.
- S26. Z. Jiang, H. Xie, S. Wang, X. Song, X. Yao and H. Wang, *Adv. Energy Mater.*, 2018, 1801433.
- S27. Y. Li, W. Zhou, S. Xin, S. Li, J. Zhu, X. Lü, Z. Cui, Q. Jia, J. Zhou and Y. Zhao, *Angew. Chem.*, 2016, **128**, 10119.

Supplementary Figures:

PEO- $\text{Al}_2\text{O}_3$ -LiTFSI  
(PAL)



PEO-PVDF- $\text{Al}_2\text{O}_3$ -LiTFSI  
(PPAL)



**Fig. S1.** Digital photos of as prepared PEO based solid electrolyte slurries with and without addition of PVDF.

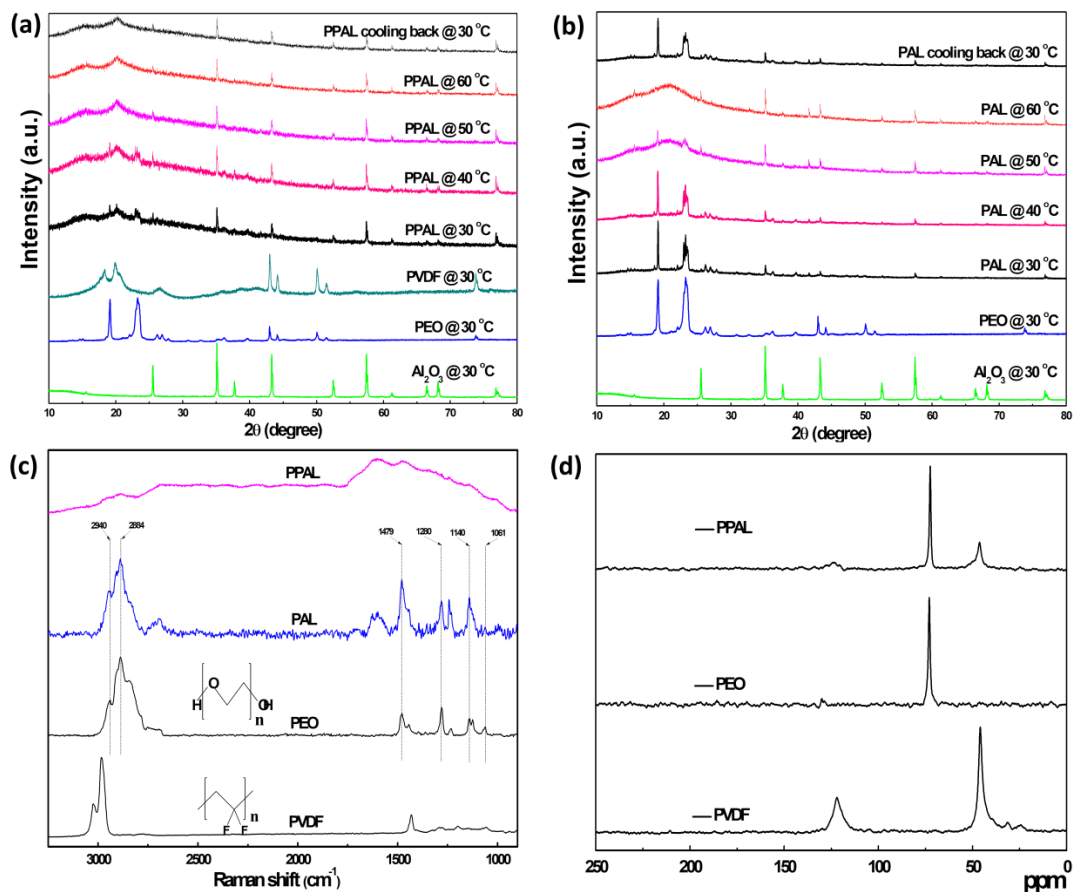


**Fig. S2.** *In situ* XRD patterns of PPAL (a) and PAL (b) solid electrolyte membranes with temperatures. (c) Raman spectra of bare PVDF, bare PEO, PPAL and PAL solid electrolyte membranes. (d) <sup>13</sup>C solid state NMR spectra of bare PVDF, bare PEO and PPAL solid electrolyte membrane.

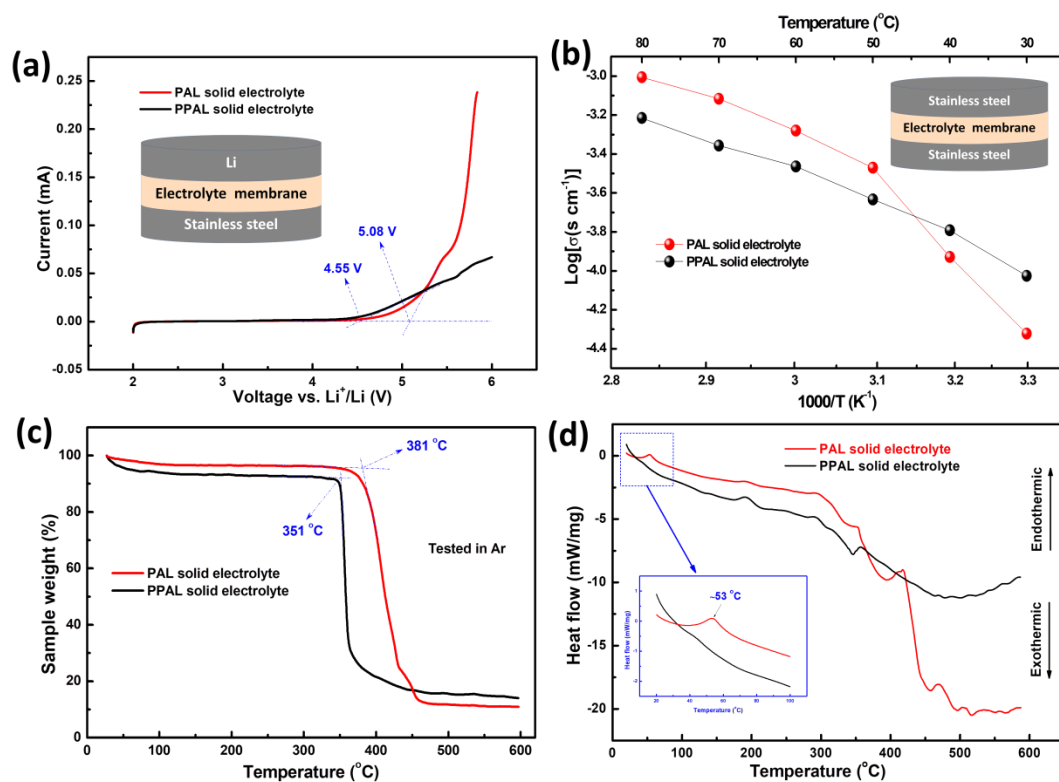


**Fig. S3.** (a) Linear sweep voltammetry (LSV) traces ( $10 \text{ mV s}^{-1}$ ) records of PPAL and PAL solid electrolyte membranes tested at  $50 \text{ }^{\circ}\text{C}$ . (b) Arrhenius plots of ionic conductivities of PPAL and PAL solid electrolyte membranes. (c) Thermogravimetric analysis (TGA) curves of PPAL and PAL solid electrolyte membranes. (d) Differential scanning calorimetry (DSC) curves of PPAL and PAL solid electrolyte membranes.

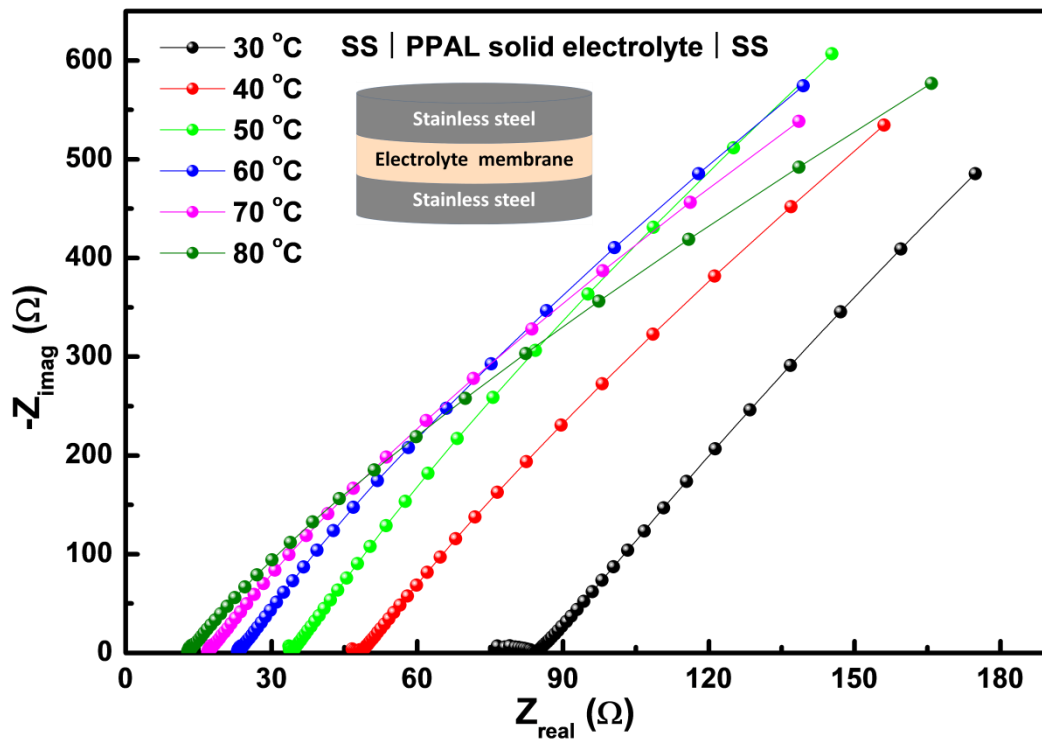


**Fig. S4.** Impedance spectra of PPAL solid electrolyte membrane measured in the form of stainless steel (SS) | electrolyte membrane | SS sandwich cell from 30 to 80 °C. ( $L_{thickness} = 0.159$  mm,  $\Phi = 16$  mm)

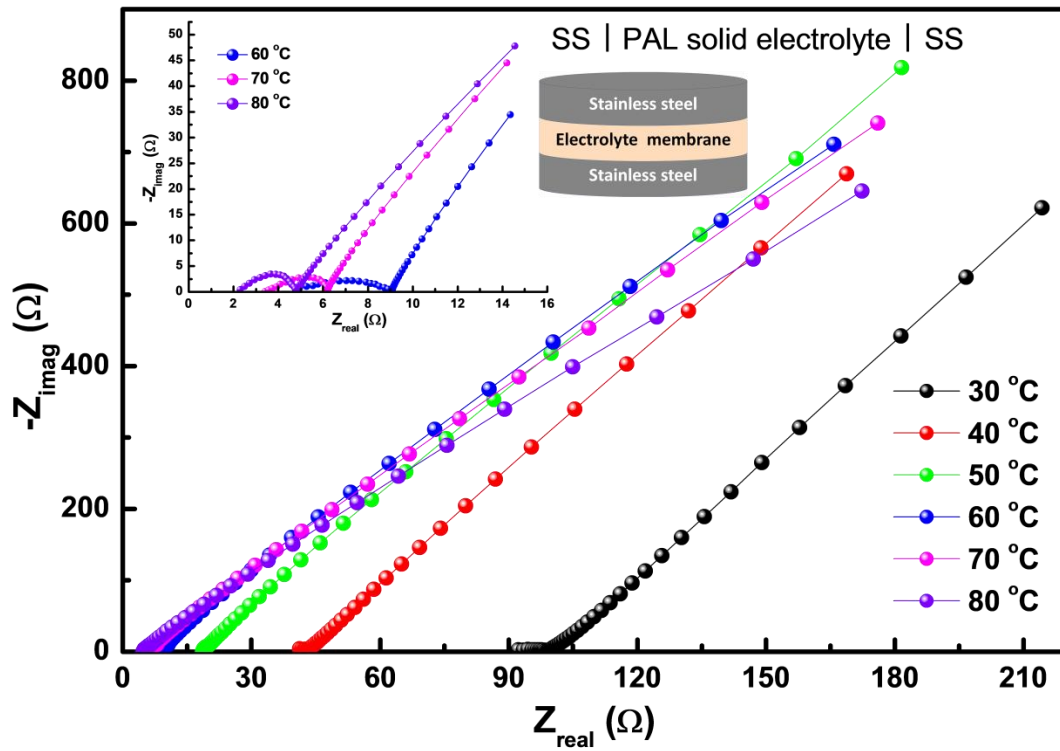


**Fig. S5.** Impedance spectra of PAL solid electrolyte membranes measured in the form of stainless steel (SS) | electrolyte membrane | SS sandwich cell from 30 to 80 °C.

( $L_{\text{thickness}} = 0.095$  mm,  $\Phi = 16$  mm)

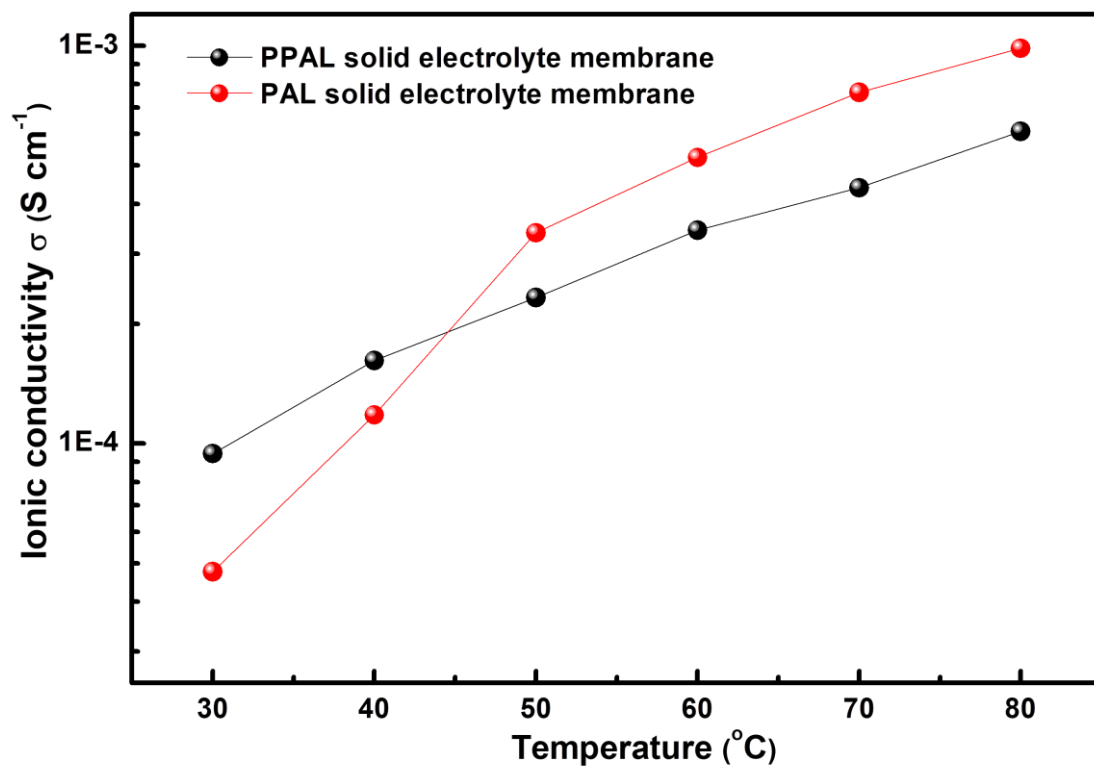


**Fig. S6.** Ionic conductivities of PAL and PPAL solid electrolyte membranes as a function of temperature.

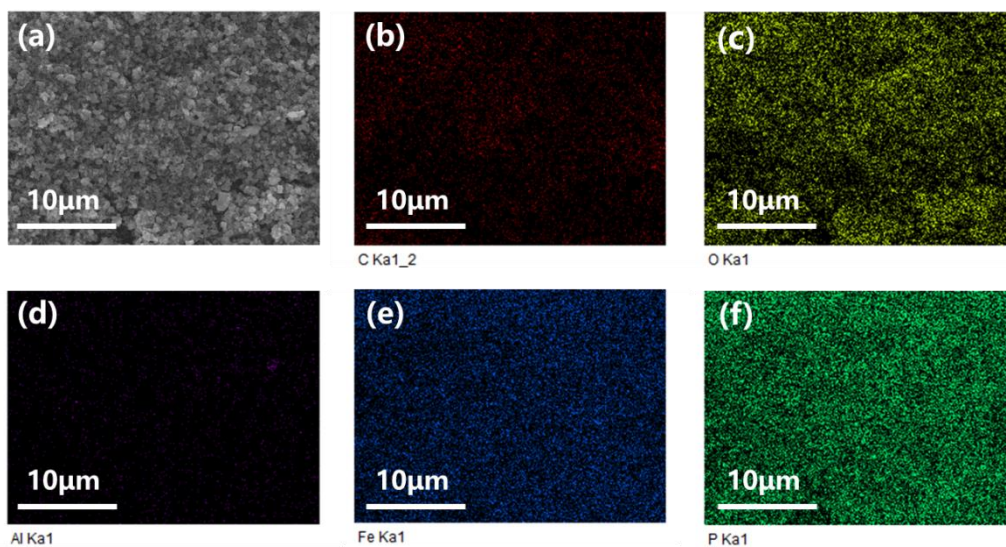


**Fig. S7.** SEM image of LiFePO<sub>4</sub> cathode tape (a), and corresponding EDS mapping images (b-f).

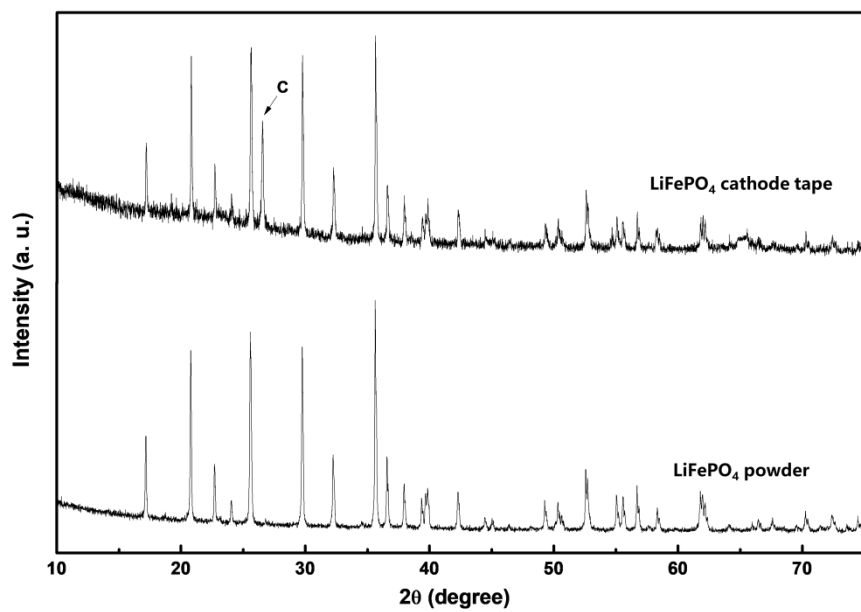


**Fig. S8.** XRD patterns of LiFePO<sub>4</sub> powder and LiFePO<sub>4</sub> cathode tape.

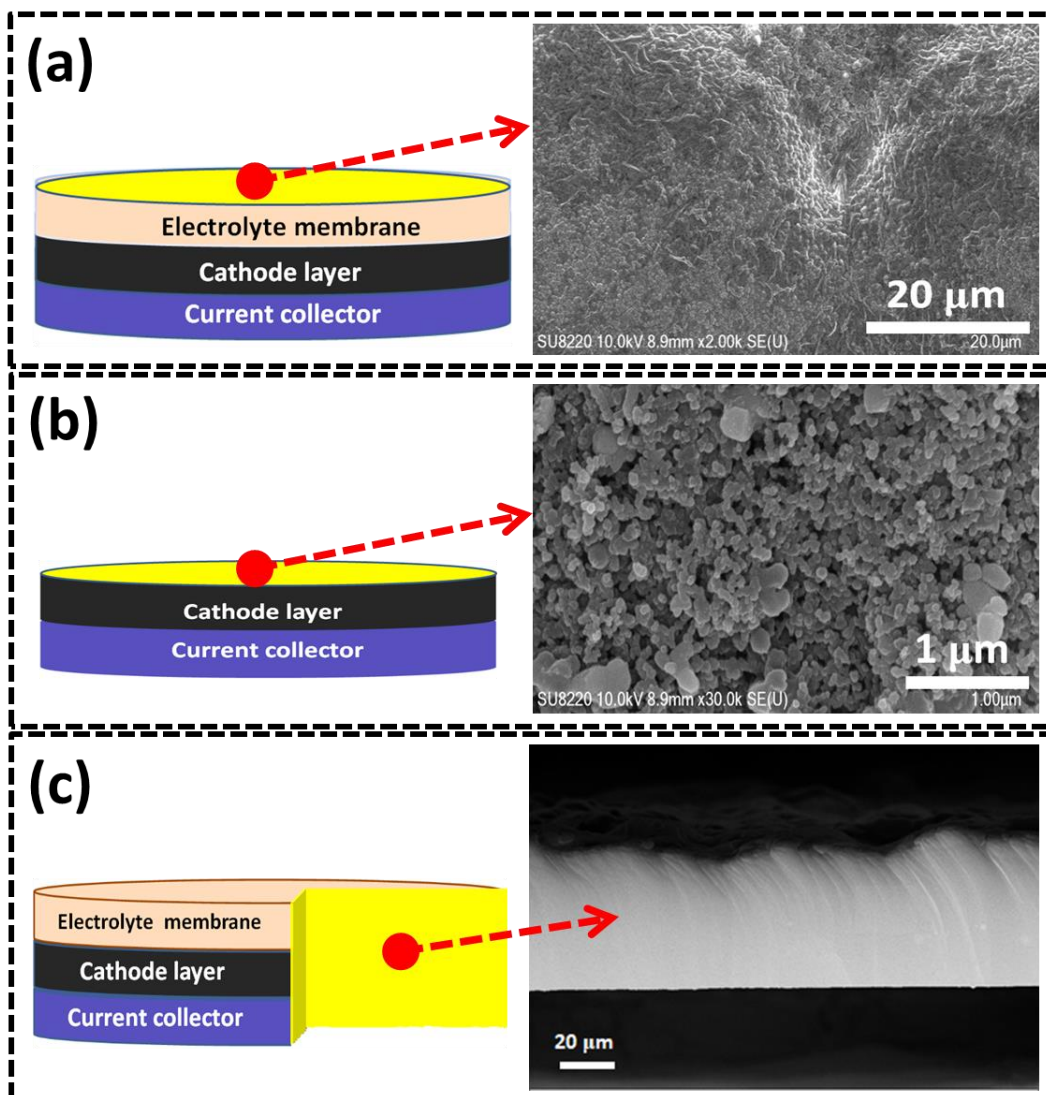


**Fig. S9.** (a) SEM image of surface morphology of the cathode supported PAL solid electrolyte membrane, (b) SEM image of surface morphology of the cathode layer, (c) SEM image of cross section of the cathode supported PAL solid electrolyte membrane.

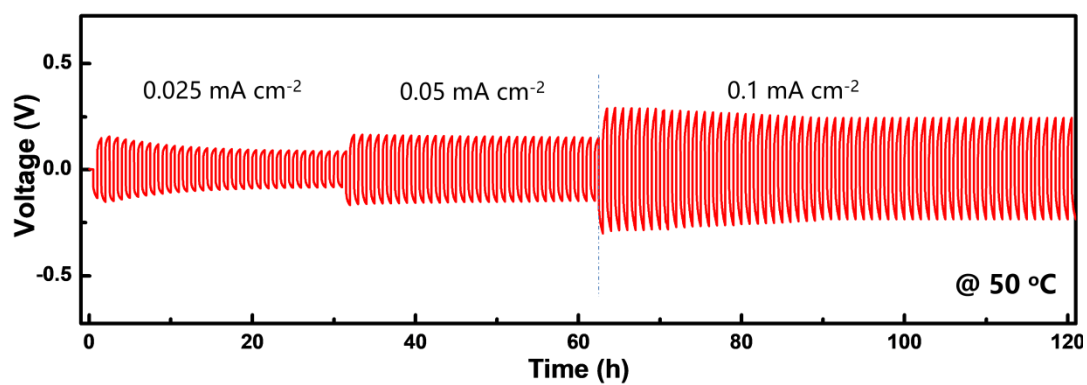


**Fig. S10.** Voltage profiles of the lithium plating/stripping in a Li-Li symmetric cell with PPAL solid electrolyte at 50 °C (0.5 h in each half cycle).

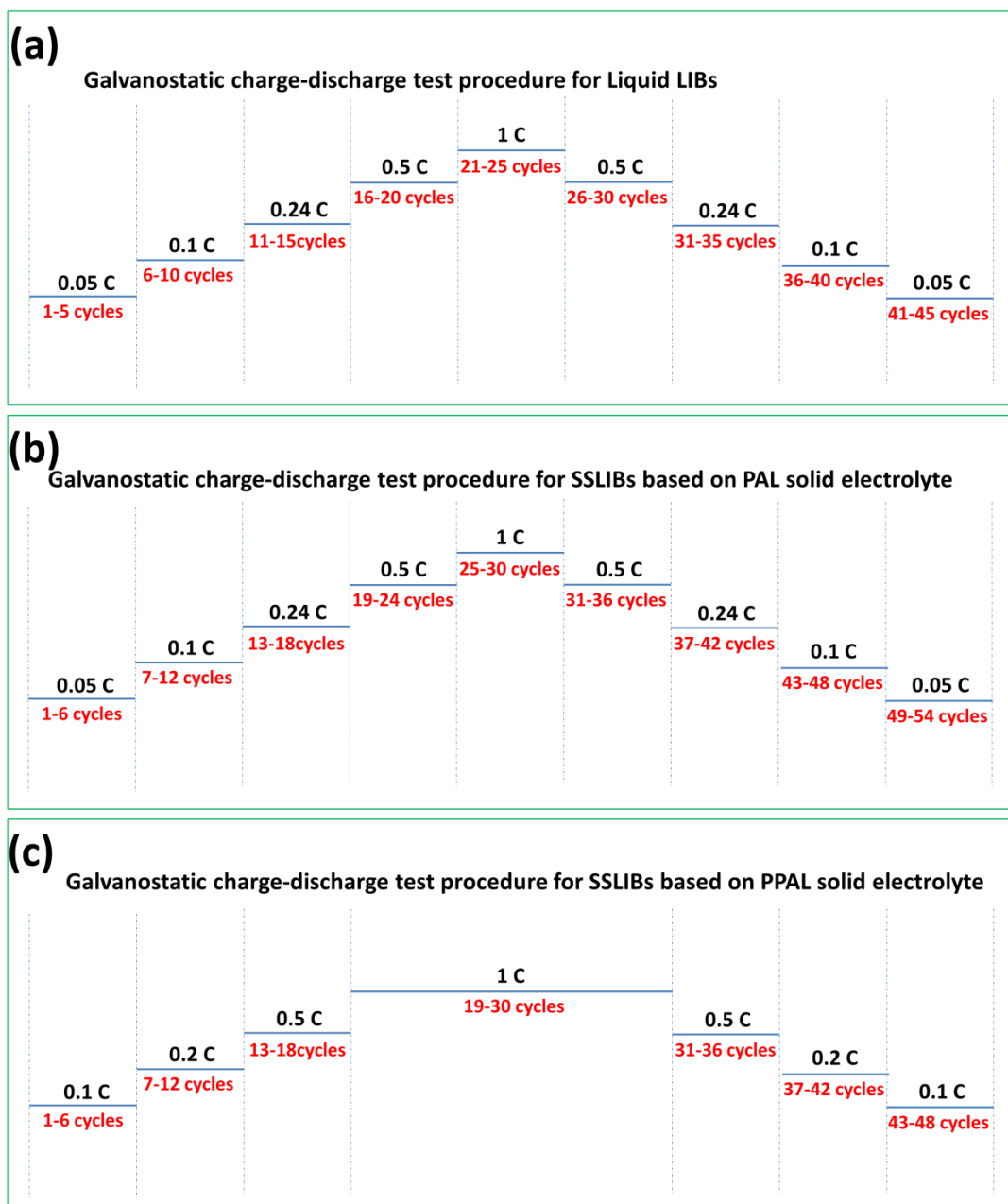


**Fig. S11.** Galvanostatic charge-discharge test procedures for liquid LIBs (a), SSLIBs based on PAL solid electrolyte (b) and SSLIBs based on PPAL solid electrolyte (c).

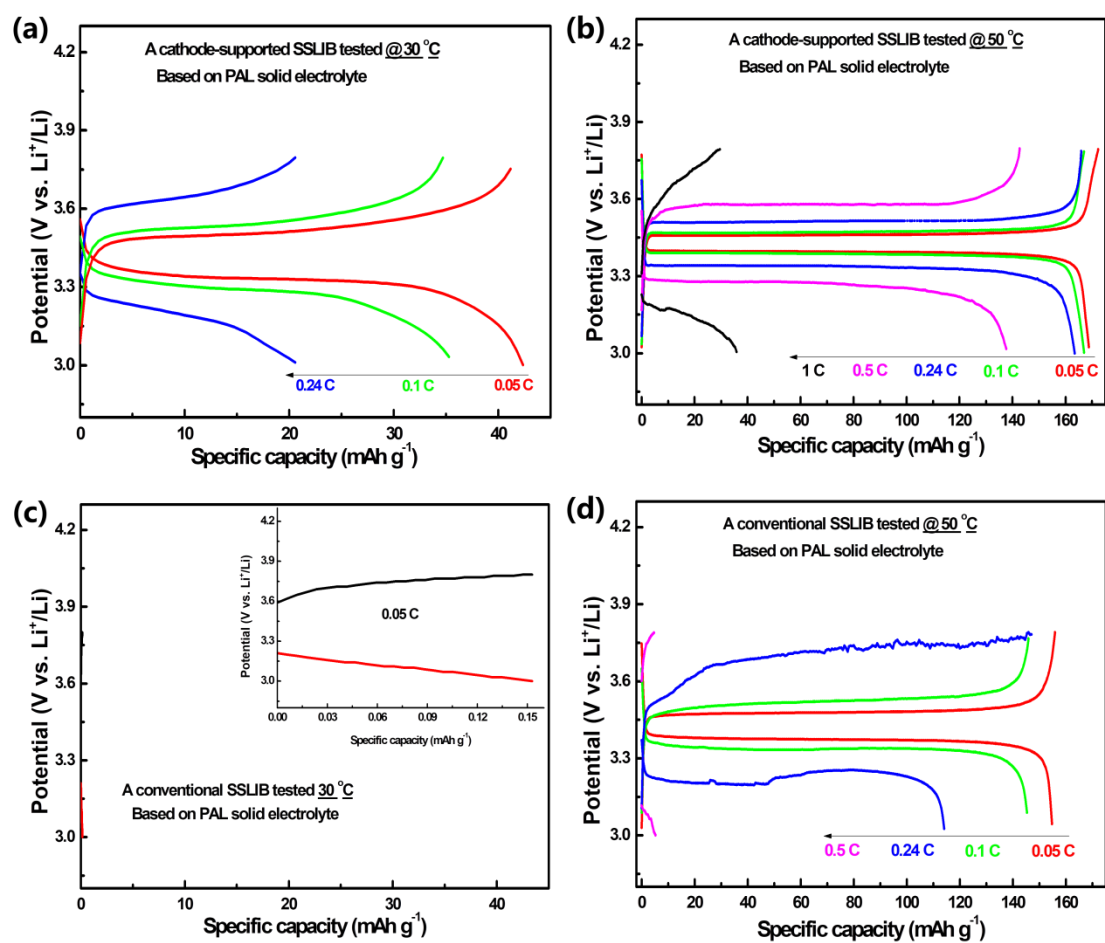


**Fig. S12.** Typical charge-discharge curves of as assembled cathode-supported SSLIBs based on PAL solid electrolyte tested at 30 °C (a) and 50 °C (b). Typical charge-discharge curves of as assembled conventional SSLIBs based on PAL solid electrolyte tested at 30 °C (c) and 50 °C (d).

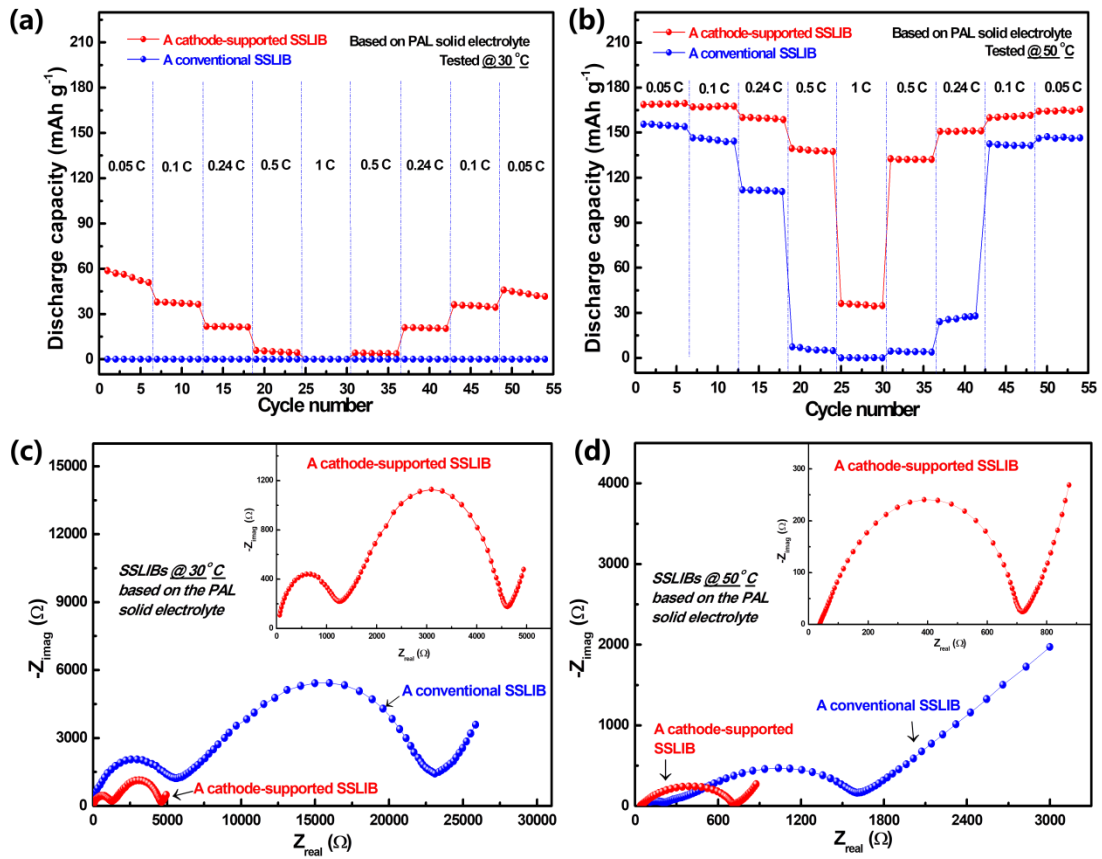


**Fig. S13.** Discharge capacities of a conventional and a cathode-supported SSLIBs based on PAL solid electrolyte tested at 30 °C (a) and 50 °C (b) as a function of cycle number at various rates. Electrochemical impedance plots of a conventional SSLIB and a cathode-supported SSLIB based on the PAL solid electrolyte at 30 °C (c) and 50 °C (d).

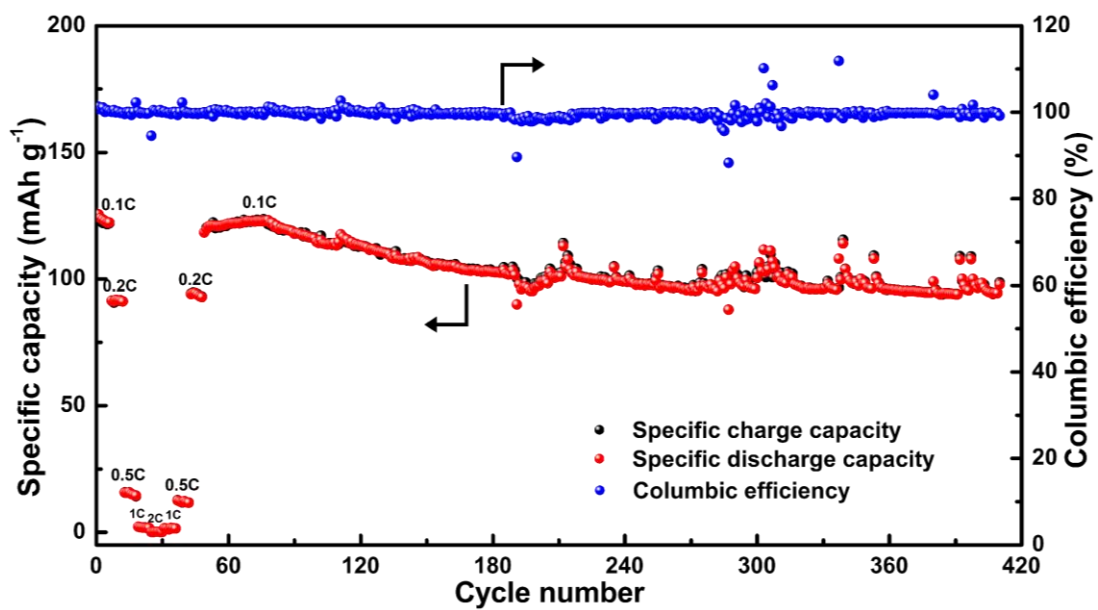


**Fig. S14.** Cyclic performance of a cathode-supported SSLIB based on PPAL solid electrolyte at 30 °C.

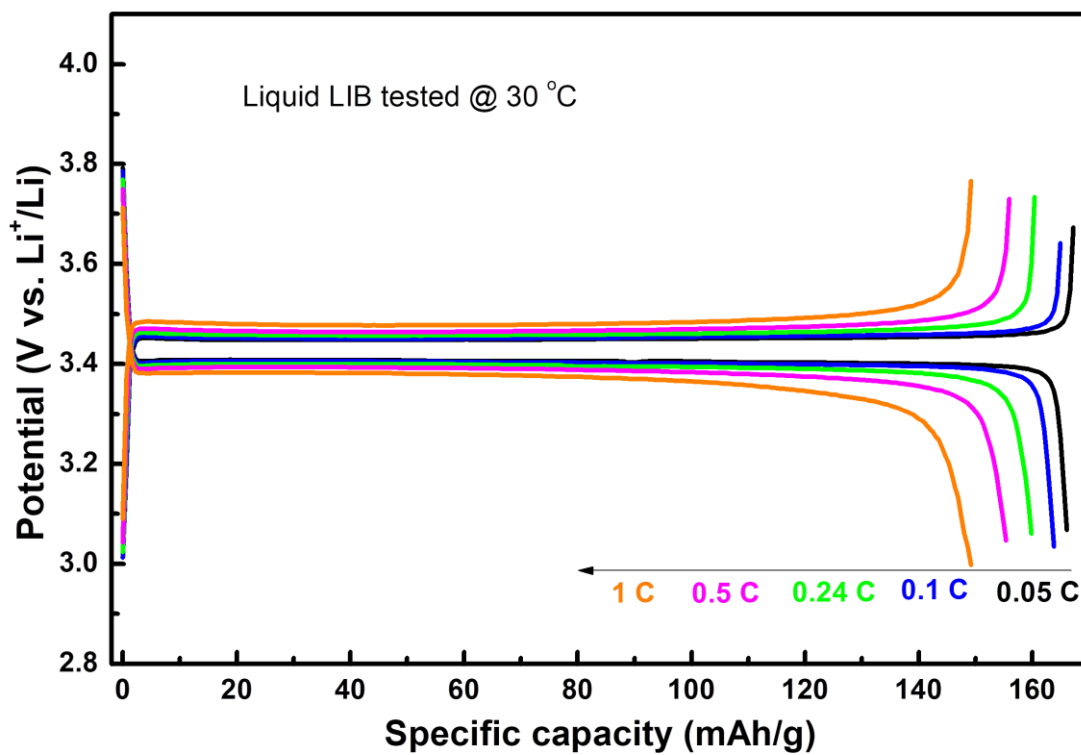
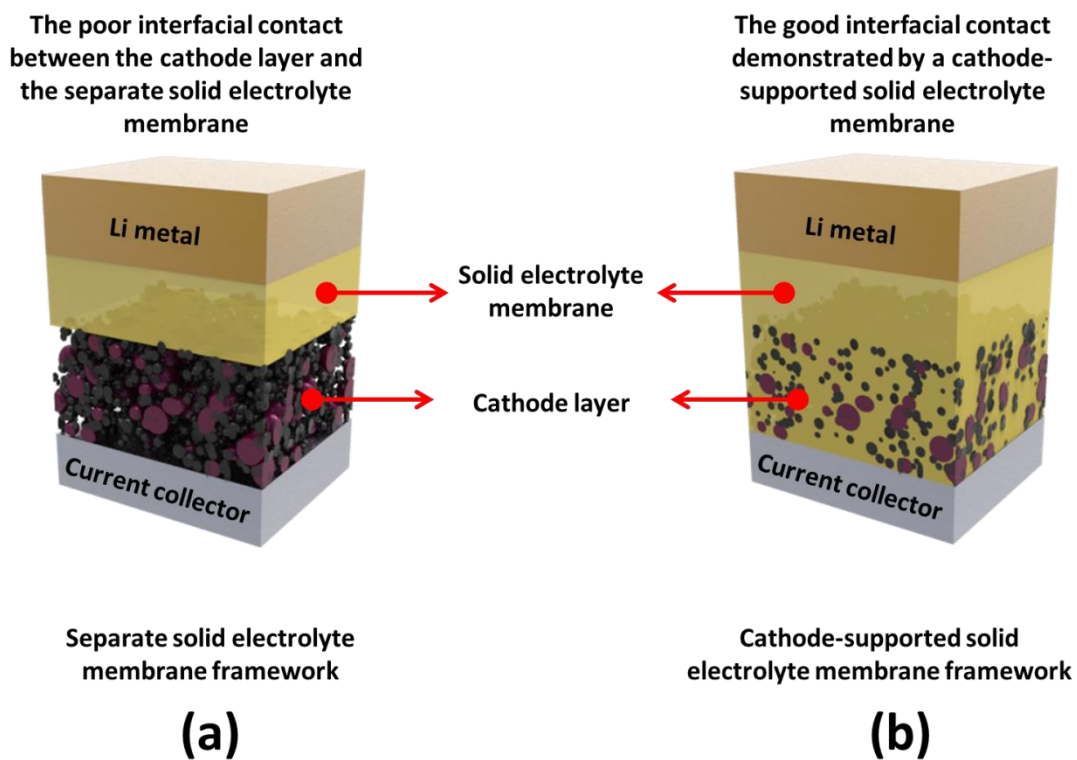
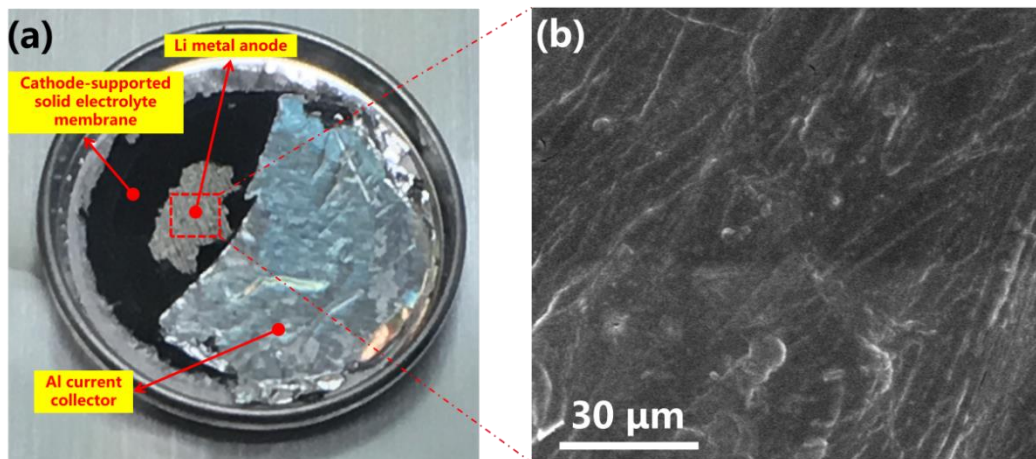


Fig. S15. Galvanostatic charge-discharge curves of a liquid LIB tested at 30 °C.



**Fig. S16.** Schematic of SSLIBs with a separate solid electrolyte membrane (a) and a cathode supported solid electrolyte membrane (b) demonstrating distinctly different interfacial contact between the cathode and the solid electrolyte.



**Fig. S17.** (a) The Digital image of a disassembled cathode-supported solid state lithium ion battery after 50 cycles galvanostatic charge-discharge test. (b) SEM image of Li metal anode.